Rock Mechanics and Rock Engineering (2021) 54:819–832
https://doi.org/10.1007/s00603-020-02305-x

ORIGINAL PAPER

An Experimental Study on the Mechanical Properties and Expansion Characteristics of a Novel Self-Swelling Cartridge for Rock Breakage

Shuai Xu[1] · Pengyuan Hou[1] · Runran Li[1] · Ming Cai[1,2,3]

Received: 19 April 2020 / Accepted: 4 November 2020 / Published online: 25 November 2020

Abstract
The application of conventional soundless (or silent) chemical demolition agents (SCDAs) is complicated and it is easy for the agents to extrude from boreholes; it is also difficult to use it in wet or up-tilt boreholes, which limits their engineering application. In this paper, the components of conventional SCDAs are optimized and an innovative SCDA cartridge is presented, which is called self-swelling cartridge (SSC). Water absorption, expansion pressure and mechanical property tests of the novel SSC after hydration reaction were carried out to investigate the expansibility and the mechanical properties of the new SSC. The test results indicate that the water absorption rate and the water absorption at full saturation decrease with the increase of the agent packing density. The recommended agent packing density is 1.65 g/cm^3, at which the immersion time and the water absorption for full saturation are 9 min and 22%, respectively. The expansion pressure of the SSC is influenced by roll diameter, agent packing density, and insertion gap. The expansion pressure is most sensitive to the insertion gap and least sensitive to the cartridge diameter. An empirical formula relating the expansion pressure and its influencing factors is presented. Both the uniaxial compressive strength and the elastic modulus of the SSC after hydration reaction increase with the increase of reaction time, while the Poisson's ratio decreases with the increase of reaction time. With the increase of confining pressure, the peak strength increases linearly, which can be described by the Mohr–Coulomb strength criterion. The novel SSC is easy to be used and the SCDA paste is less likely to be extruded from boreholes. It can be applied to fracturing rock masses using boreholes in any inclination, dry or wet. This is important for broadening the application of SCDA.

Keywords Soundless chemical demolition agent (SCDA) · Self-swelling cartridge (SSC) · Rock fracturing · Hydration reaction · Water absorption · Expansion pressure · Strength

1 Introduction

Soundless chemical demolition agents (SCDAs) are superfine powder-like gelling material with excellent expansion properties (Harada et al. 1989). When a SCDA is inserted or placed into a borehole, it expands after hydration reaction, which applies an expansion pressure to the borehole wall. Rock fracturing occurs when the expansion pressure reaches the limit above which tensile fractures initiate in the direction perpendicular to the minimum principal stress (Chatterji and Jeffery 1966; Kasai 1989; Swanson and Labuz 1999). Compared with the conventional drill-and-blast excavation method, rock breakage using SCDAs has the advantages of no vibration, no noises, no flying rocks, higher safety, and lower cost (Laefer et al. 2010; De Silva et al. 2016). Compared with hydraulic fracturing, fracturing rocks using SCDAs is easy and the cost is low (He et al. 2016, 2017). Since 1970s, SCDAs have been widely used for rock fracturing (Arshadnejad et al. 2011), demolition of concrete foundation (Laefer et al. 2010; De Silva et al. 2016), coal mining (Xu et al. 2015; Zhai et al. 2018), and shale gas extraction (Guo et al. 2015a, b). In recent years, the application of SCDA has been extended to ground control (Li et al. 2018) and rock bolting (Xu et al. 2019).

✉ Pengyuan Hou
neuhpy@163.com

✉ Ming Cai
mcai@laurentian.ca

[1] Key Laboratory of Ministry of Education on Safe Mining of Deep Metal Mines, Northeastern University, Shenyang 110819, People's Republic of China

[2] Bharti School of Engineering, Laurentian University, Sudbury, ON, Canada

[3] MIRARCO, Laurentian University, Sudbury, ON, Canada

However, conventional SCDAs have some shortcomings in engineering application. First, powder-like SCDAs need to be converted into a paste form for field application, which requires complicated field operation procedures (Ramachandran et al. 1964; Chatterji 1995; Kim et al. 2018; Shang et al. 2018; Zhai et al. 2018). Second, it is difficult to use SCDA pastes in boreholes containing water because the water content of the SCDA paste can be changed, which reduces the effectiveness of the SCDAs (Gambatese 2003; De Silva et al. 2019). Third, SCDA pastes are difficult to be applied in up-tilt boreholes due to gravity flow, which limits its application. Lastly, materials of conventional SCDAs can be extruded from a borehole due to fast hydration reaction, which can reduce the effectiveness of the agent in rock fracturing (Ba and Liu 1988; Xie et al. 2018).

To overcome the shortcomings mentioned above, some researchers packaged SCDA powders into bags for field application (Kasama et al. 1983). Permeable bags containing tightly packed SCDA powders are immersed in water for some time and then placed into a borehole. A stick with a point head is used to send the SCDA bags to pre-defined locations, and then the SCDA bags are squashed. The SCDA powders expand after the hydration reaction, generating a large expansion pressure which could fracture the rock mass. Although SCDA bags can be used in up-tile boreholes, it is hard to control the agent packing density. In addition, the water content of the SCDA is also difficult to be maintained in boreholes containing water, and the SCDA paste is easy to be extruded from the boreholes. Hence, the efficiency of using SCDA bags to fracture rock varies considerably.

In this paper, the component of conventional SCDAs is modified to solve the problems encountered in the applications of conventional SCDA pastes and bags. Binder, water-retaining agent, and inertia materials are added to control the rate of hydration reaction. An innovative self-swelling cartridge (SSC) with axial restraint is designed to prevent the agent from extruding from boreholes. Water absorption, expansion pressure and mechanical property tests of the SSCs after hydration reaction were carried out to reveal their expansion characteristic and the mechanical properties. Water absorption ratios and water immersion time for full saturation of the SSCs with different agent packing densities were obtained. Factors that influence expansion pressure are quantitatively analyzed. The effects of hydration reaction time on uniaxial compressive strength (UCS), elastic modulus, Poisson's ratio, and expansion pressure of the SSCs are studied. In addition, parameters of the Mohr–Coulomb strength criterion for the material of the SSC are determined based on the triaxial compression test results.

2 Experimental Program

2.1 Materials

The SCDA used in our study is a superfine power-like material, mainly consisting of C_3S ($3CaO{\cdot}SiO_2$), C_2S ($2CaO{\cdot}SiO_2$), C_4AF ($4CaO{\cdot}Al_2O_3{\cdot}Fe_2O_3$), and light-burned calcium oxide (f-CaO). When the SCDA powder contacts with water, the minerals that cover the surface of f-CaO hydrate and generate C–H–S ($3CaO{\cdot}2SiO_2{\cdot}3H_2O$), C_3FH_6 ($3CaO{\cdot}Fe_2O_3\ 6H_2O$), and C_3AH_6 ($3CaO{\cdot}Al_2O_3{\cdot}6H_2O$) (You 2008; Dai 2016). These hydrates have cementation capacity and provide the strength for the SCDA. When CaO contacts with water, it generates $Ca(OH)_2$ crystals after hydration reaction. With continuous generation of $Ca(OH)_2$ crystals, the volume of the solid increases, leading to the expansion of the SCDA (Ramachandran et al. 1964; Chatterji and Jeffery 1966; Harada et al. 1989, 1993; Chatterji 1995; De Silva et al. 2017). If the hydration reaction occurs in an unrestricted space, the hydrates will crack and finally become a powder-like loose material. However, if the hydration reaction occurs in a restricted space, the hydrates will generate an expansion pressure against the constraining boundaries.

In field applications, due to the fast rate of hydration reaction, the water content and the cohesion of the SCDA decease with water evaporation. The SCDA paste is likely to leak from the borehole, leading to a low efficiency of rock fracturing (Swanson and Labuz 1999; Étkin and Azarkovich 2006; Huynh and Laefer 2009). In this study, povidone binder, polymer resin water-retaining agents (aquasorb), sand (inert material), and starch (disintegrant) are added to the SCDA to adjust the rate of hydration reaction of the SCDA, control the water content, and improve the cohesion so as to prevent SCDA pastes from leaking from the boreholes. The components of the improved SCDA are listed in Table 1.

2.2 Structure Design of SSC

For easy and effective field application of SCDAs, we developed a self-swelling cartridge (SSC). A SSC is mainly composed of SCDAs, permeable paper, and sponge, a thread rod, two gaskets, two plates, and two plate nuts. Figure 1a presents the structure of the SSC with a diameter of 50 mm and a length of 100 mm. The packing cover is made of

Table 1 Composition of raw materials of SSC cartridge

CaO (%)	Binder (%)	Aquasorb (%)	Inert material (%)	Disintegrant (%)
60–70	10–15	2–5	2–6	1–4

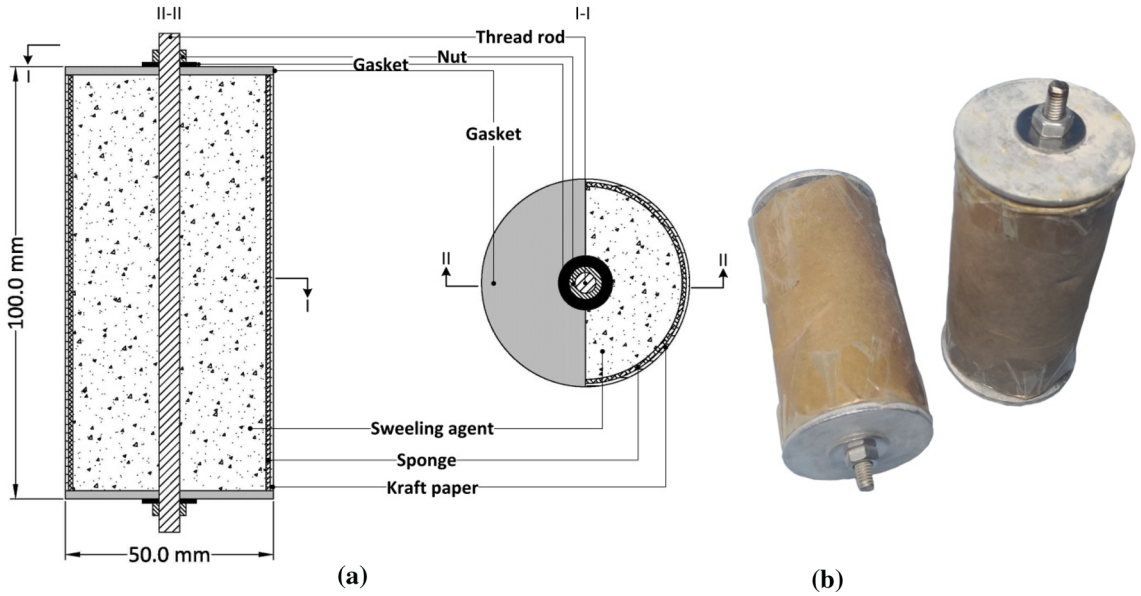

Fig. 1 **a** Structure of SSC and **b** examples of SSC

kraft paper and sponge with thicknesses of 0.8 and 1.0 mm, respectively. The self-swelling powder is mixed with a moderate amount of binder, aquasorb, and inert material and then filled into the packing cover. The mixture is tightly compressed and packed manually or using a machine. The density of the packed roll agent is normally in the range of 1.65–2.05 g/cm^3. A 5.0-mm diameter thread rod passes through the center of the gasket and the cartridge, which is assembled with the plates, gaskets, and nuts. Figure 1b shows two examples of the SSCs used in the experiments conducted in this study.

2.3 Test Methods

2.3.1 Water Absorption Test

Water absorption properties of the SSC include water absorption and water absorption rate. The water absorption determines the water to cement ratio of the SSC, which influences the expansion pressure. The water absorption rate determines the time needed to fully saturate a SSC in water. If the immersion time is too short, the water absorption is low and the SSC cannot react with water completely, which can reduce the expansion of the SCDA. If the immersion time is too long, hydration reaction can occur before a SSC is inserted into a borehole, which can lead to poor rock fracturing. In addition, the time needed to fully saturate a SSC depends on the agent packing density. Hence, immersion times of the SSCs with different agent packing densities needs to be determined by the water absorption test.

SSCs with a dimension of 50 mm (diameter) × 100 mm (length) were used for the water absorption tests. Three cartridge densities, 1.65, 1.85, and 2.05 g/cm^3, were considered. A SSC was immersed in the 20 °C water and then taken out at a 50-s interval and the weight of the saturated SSC was measured. A water absorption test was terminated when the change of the weight of the cartridge was less than 0.5 g in three consecutive measurements. Three tests for each packing density case were conducted.

2.3.2 Expansion Pressure Test

Expansion pressure is a key index to evaluate the expansion characteristics of the SSC, and it is affected by many factors such as roll diameter, agent packing density, and installation gap. The roll diameter and the agent packing density control the amount of SCDAs and the water to cement ratio, which in turn affect the expansion pressure of the SSC. The installation gap between the roll and the borehole affects the easiness of installation and expansion pressure of the SSC. The larger the installation gap, the easier it is to install the cartridge and the smaller the expansion pressure will be. In this case, expansion-induced cracking will be less. On the other hand, the smaller the installation gap is, the more difficult it is to install the SSC but the expansion pressure is higher. Therefore, it is necessary to carry out the expansion pressure test of the SSCs considering different roll diameters, agent packing densities, and installation gaps. The test scheme is shown in Table 2. SSCs with different agent packing densities were immersed in 20 °C water, and after water absorption saturation was reached, the expansion pressure

Table 2 Test cases for studying the influence of roll diameter, agent packing density, and insertion gap on expansion pressure

Specimen #	Roll diameter (mm)	Agent packing density (g/cm^3)	Hole diameter (mm)	Installation gap (mm)
A-#1	40.0	1.65	42.0	1.0
A-#2	40.0	1.85	52.0	6.0
A-#3	40.0	2.05	47.0	3.5
A-#4	45.0	1.65	52.0	3.5
A-#5	45.0	1.85	47.0	1.0
A-#6	45.0	2.05	57.0	6.0
A-#7	50.0	1.65	52.0	1.0
A-#8	50.0	1.85	57.0	3.5
A-#9	50.0	2.05	52.0	1.0

test was conducted based on the method described in literature (Deighton 1976; Pawlik and Reisman 1980; Hertzberg and Saunders 1985).

The expansion pressure of a SSC is calculated by applying the theory of elasticity to a stainless-steel cylinder, based on the theory of thick-wall cylinders (Pawlik and Reisman 1980; Hertzberg and Saunders 1985; Lawn 1993). Under the loading condition of uniform internal and external pressures, the radial and tangential stresses of a thick-wall steel cylinder are given by

$$\sigma_r = -\frac{\frac{b^2}{r^2}-1}{\frac{b^2}{a^2}-1}\times P_a - \frac{1-\frac{a^2}{r^2}}{1-\frac{a^2}{b^2}}\times P_b, \tag{1}$$

$$\sigma_\varphi = \frac{\frac{b^2}{r^2}+1}{\frac{b^2}{a^2}-1}\times P_a - \frac{1+\frac{a^2}{r^2}}{1-\frac{a^2}{b^2}}\times P_b, \tag{2}$$

where σ_r and σ_φ are the compressive and tensile stresses, respectively, r is the radial distance from the center of the thick-wall steel cylinder, a and b are the inner and outer radii of the cylinder, P_a and P_b are the internal and external pressures acting on the cylinder, respectively. During a expansion pressure test, the pressure acting on the outer wall is $P_b=0$ at $r=b$; thus, Eqs. (1) and (2) can be simplified to:

$$\sigma_\varphi = \frac{2a^2}{b^2-a^2}\times P_a. \tag{3}$$

The tangential and axial stresses in a small unit on the outer wall of the expansion pressure testing device satisfy the condition of plane stress. The generalized Hooke's law in the polar coordinate system is written as

$$\begin{cases} \varepsilon_\varphi = \frac{1}{E}\left(\sigma_\varphi - \mu\sigma_a\right) \\ \varepsilon_a = \frac{1}{E}\left(\sigma_a - \mu\sigma_\varphi\right) \end{cases}. \tag{4}$$

Combining Eqs. (3) and (4) leads to

$$P = P_a = \frac{E\left(k^2-1\right)}{2\left(1-\mu^2\right)}\left(\varepsilon_\varphi + \mu\varepsilon_a\right), \tag{5}$$

where P and P_a are the expansion pressure and internal expansion pressure of the SSC, respectively, E is the elasticity modulus of the steel cylinder (with a value of 206 GPa), μ is the Poisson's ratio of the steel cylinder (with a value of 0.3), k is the ratio of outer to inner radii, and ε_φ and ε_a are the circumferential and axial strains, respectively, of the thick-wall steel cylinder. By measuring the circumferential and axial strains resulted from the expansion of the SCDA on the surface of the cylinder, the expansion pressure P can be calculated using Eq. (5). The strains are measured using strain gauges glued on the outer surface of the steel cylinder (Harada et al. 1993; China 2008; De Silva et al. 2017).

2.3.3 Mechanical Property Test After Hydration Reaction

A specimen preparation equipment was designed for the hydration reaction of the SSC and to provide a constraint space for the hydration swelling of a SSC and for taking out the SSC specimen after hydration reaction. The equipment consists of a split steel pipe with a wall thickness of 5.0 mm, circumferential restraint hoops, pressure pads at both ends, and threaded rods with clamp nuts (Fig. 2). The gap between the SSC and the steel pipe is 1 mm. Before a test, the SSC (with a dimension of 50 mm (diameter) × 100 mm (length) and an agent packing density of 1.65 g/cm^3) was immersed in 20 °C water. After the SSC was fully saturated, it was placed into the specimen preparation equipment for hydration reaction. After the completion of the hydration reaction at a specified time, the threaded rods and the circumferential restraint hoops were removed to get the SSC specimen. Finally, the physical properties of the SSC specimens were tested, including the mass and the longitudinal wave velocity. To reduce the dispersion of the test results, SSC specimens with similar physical properties were selected to perform uniaxial and conventional triaxial compression tests.

The RockMan-207 triaxial compression test machine (Fig. 3), developed by Northeastern University, China, was used to conduct the compression tests. The frame stiffness, maximum axial loading force, and maximum confining pressure of the machine are 5 GN/m, 2000 kN, and 100 MPa, respectively. Three types of loading control methods, i.e., load-controlled, axial-displacement-controlled, and circumferential-displacement-controlled loadings are available. Two axial linear variable differential transducers (LVDTs) and one circumferential LVDT were used to measure the axial and circumferential deformations. The measurement range and precision of the LVDTs are ± 6.25 mm and 0.05%, respectively.

The test schemes for the compression tests of the SSC specimens with different hydration reaction times and confining pressures are shown in Table 3. The experimental procedure and result calculation follow the ISRM-suggested methods (Kovari et al. 1983; Fairhurst and Hudson 1999). Since the SSC specimens show ductile and large deformations, to obtain complete stress–strain curves of the specimens, the axial-displacement-controlled loading was used in the early stage of loading with an axial strain rate of 1×10^{-3}/s until the stress reached 70% of the peak strength. Then, the axial strain rate was changed to 1×10^{-6}/s until the stress decreased to 50% of the peak strength. After that, the axial strain rate was increased to 1×10^{-3}/s again until the stress reached the residual strength of the specimen or the strain reached the measurement range of the LVDT. Five specimens were tested in each test scenario.

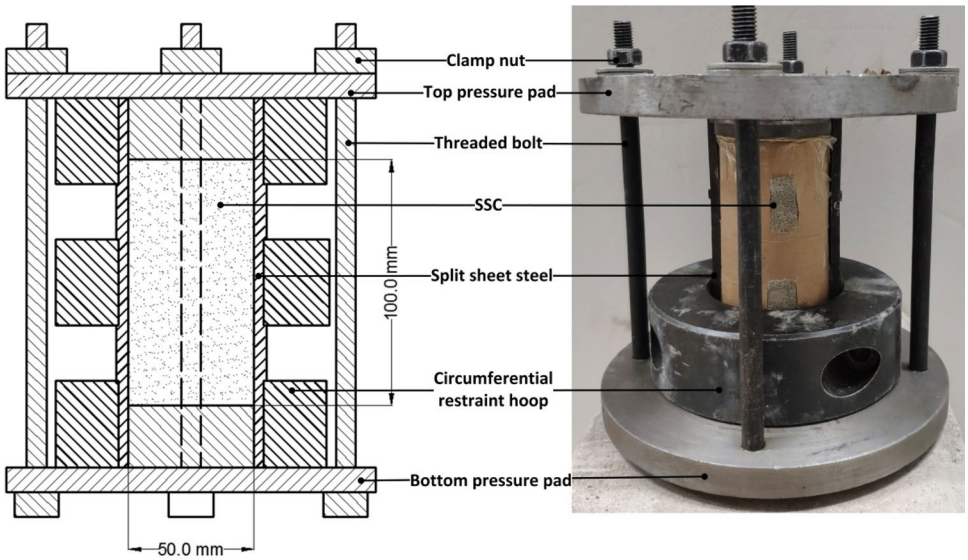

Fig. 2 Test specimen preparation device

Fig. 3 RockMan-207 triaxial compression test machine

Table 3 Test cases for different confinements and hydration reaction times

Specimen #	B-#1	B-#2	B-#3	B-#4	B-#5	B-#6	B-#7	B-#8	B-#9	B-#10
Confining pressure (MPa)	0	0	0	0	0	0	1	5	10	20
Hydration reaction time (h)	4	6	8	10	16	24	24	24	24	24

3 Test Results

3.1 Water Absorption Test Results

The water absorptions of the SSCs with different agent packing densities at different immersion times are presented in Fig. 4. For the agent packing densities of 1.65, 1.85, and 2.05 g/cm^3, the immersion times required for the SSCs to become fully saturated are 9, 10, and 13 min, respectively. The corresponding water absorptions of these SSCs are 22%, 21%, and 20%, respectively. The test results indicate that the water absorption and water absorption rate of the SSCs decrease gradually as the agent packing density increases. A higher agent packing density results in a lower internal porosity, which can lead to a decrease of water absorption and the water absorption rate. The water absorption of a fully saturated SSC specimen after hydration reaction determines the water to cement ratio. When the water to cement ratio is 25%, the agent has the highest utilization rate and the best expansion effect (De Silva et al. 2016). To ensure that the water to cement ratio of the SSC approaches the optimal value, and with the consideration of cost, the utilization ratio and the absorption rate of the SCDAs, the recommended agent packing density, immersion time, and water absorption of fully saturated SSCs are 1.65 g/cm^3, 9 min, and 22%, respectively.

3.2 Expansion Pressure Test Results

The expansion pressure test results of the SSCs with different roll diameters, agent packing densities and insertion gaps are presented in Fig. 5. When the agent packing density and the insertion gap are kept constant, the expansion pressure is positively related to the roll diameter. The test results of Specimens A-#1 and A-#7 show that when the agent packing density and the insertion gap are 1.65 g/cm^3 and 1.0 mm, respectively, the expansion pressure increases from 14.7 to 20.5 MPa when the roll diameter increases from 40 to 50 mm. If the roll diameter and the insertion gap are kept constant, the expansion pressure increases as the agent packing density increases. The test results of Specimens A-#7 and A-#9 show that when the roll diameter and the insertion gap are 50 mm and 1.0 mm, respectively, the expansion pressure increases from 20.5 to 52.3 MPa when the agent packing density increases from 1.65 to 2.05 g/cm^3.

The test results of Specimens A-#1 and A-#6 show that when both the roll diameter and the agent packing density increase, the expansion pressure decreases as the insertion gap increases. The expansion pressure reaches 14.7 MPa when the agent packing density, roll diameter, and insertion gap are 1.65 g/cm^3, 40 mm, and 1.0 mm, respectively. The expansion pressure decreases to 2.3 MPa when the agent packing density, roll diameter, and insertion gap are 2.05 g/cm^3, 45 mm, and 6.0 mm, respectively. It is seen that compared with roll diameter and agent packing density, the insertion gap has a larger effect on the expansion pressure. The test results of Specimens A-#5 and A-#7 show that for a given insertion gap, the expansion pressure decreases when the roll diameter is increased while the agent packing density is decreased. When the roll diameter is increased from 40 to 45 mm and the agent packing density is decreased from 1.85

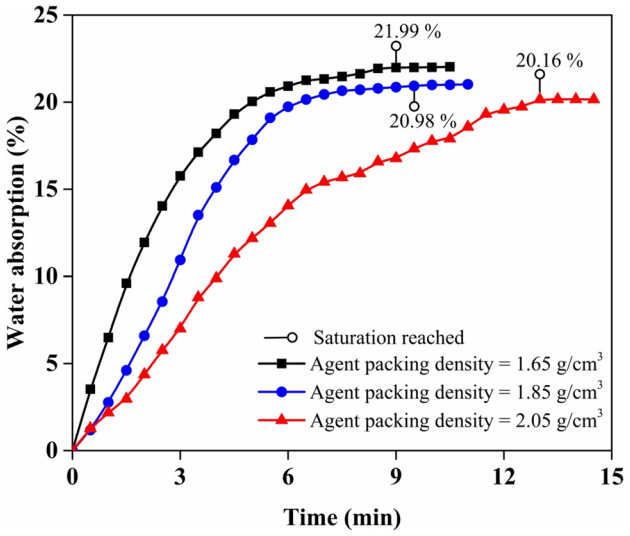

Fig. 4 Water absorption of SSCs with different agent packing densities

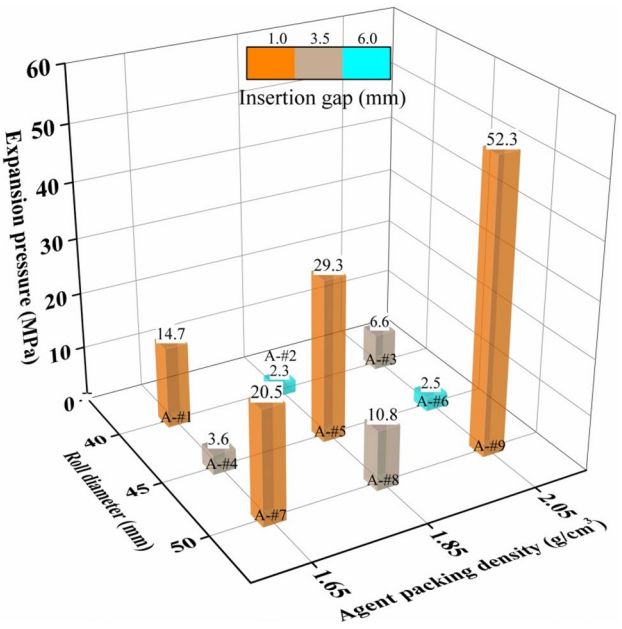

Fig. 5 Influence of roll diameter, agent packing density, and insertion gap on expansion pressure

to 1.65 g/cm^3, the expansion pressure decreases from 29.3 to 20.5 MPa. Hence, the expansion pressure is more sensitive to the agent packing density than to the roll diameter.

In summary, the expansion pressure of a SSC is influenced by roll diameter, agent packing density, and insertion gap. Among them, it is more sensitive to insertion gap, followed by agent packing density, and is less sensitive to roll diameter.

3.3 Uniaxial Compression Test Results

Complete stress–strain curves under uniaxial compression and photos of the failed SSC specimens at different hydration reaction times are presented in Fig. 6. The dimensions of the specimens are 50 mm in diameter and 100 mm in length, with an agent packing density of 1.65 g/cm^3.

When the hydration reaction time is 4 h, the UCS (σ_c), peak strain (the strain that corresponds to the peak strength), elastic modulus (E), and Poisson's ratio (ν) of the SSC specimens are 1.2 MPa, 1.276%, 0.20 GPa, and 0.30, respectively. The photo of the tested specimen shows that there are several distinct fractures, one main fracture propagating through the specimen, one local axial fracture and one circumferential fracture at each end of the specimen. The failure modes are splitting failure. When the hydration reaction time is increased to 24 h, the UCS and the elastic modulus increase to 9.6 MPa and 1.24 GPa, respectively, while the peak strain and the Poisson's ratio decrease to 0.926% and 0.18, respectively. In this case, two main fractures propagate through the specimen, and three local axial fractures and two local circumferential fractures occur at each end of the specimen. The failure mode is also splitting failure, showing a more characteristic brittle failure with spalling of some small fragments during the test. Overall, with the increase of the hydration reaction time, the UCS and the elastic modulus of the SSC specimens increase and its peak strain and Poisson's ratio decrease gradually. The failure modes are splitting failure. In addition, the number of fractures increases and brittle failure becomes more noticeable.

3.4 Triaxial Compression Test Results

Complete stress–strain curves under triaxial compression and photos of the failed SSC specimens (with a diameter of 50 mm, a length of 100 mm and an agent packing density of 1.65 g/cm^3) after 24 h hydration reaction are shown in Fig. 7.

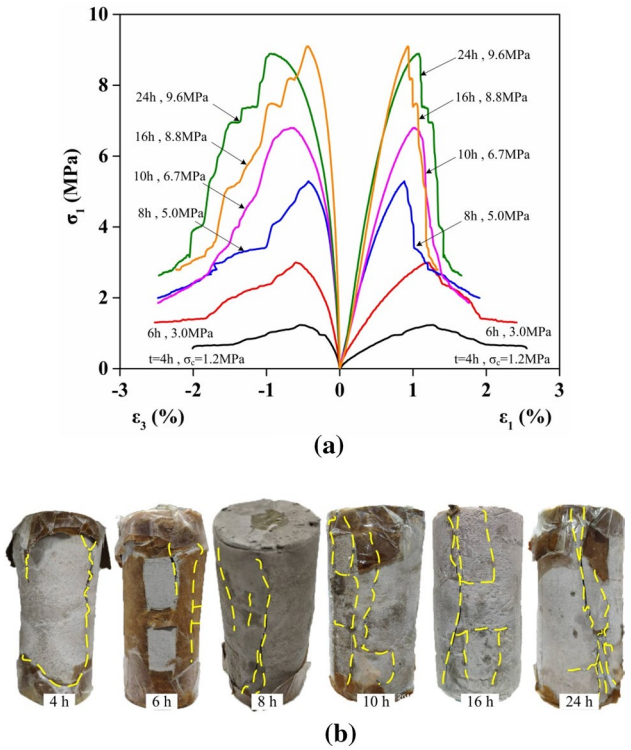

Fig. 6 **a** Complete stress–strain curves and **b** failure modes of SSC specimens under uniaxial compression, with different hydration reaction times. ε_1, ε_3, σ_1 and t are axial strain, lateral strain, axial stress and hydration reaction time, respectively

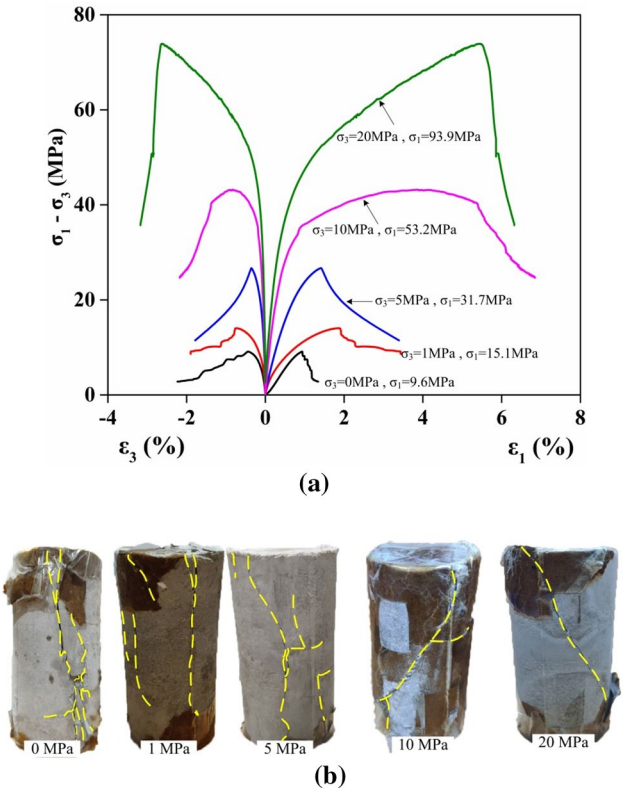

Fig. 7 **a** Complete stress–strain curves and **b** failure modes of SSC specimens under triaxial compression, with a hydration reaction time of 24 h. ε_1, ε_3, σ_1 and σ_3 are axial strain, lateral strain, axial stress and confining pressure, respectively

At 1.0 MPa confining pressure, the peak strength (σ_1) of the specimen is 15.1 MPa and the failure mode is splitting failure. At 5.0 MPa confining pressure, the peak strength is 31.7 MPa and both splitting and shear failures occur in the specimen. When the confining pressure is 10.0 MPa, the peak strength increases to 53.2 MPa and the specimen fails in shear. At 20.0 MPa confining pressure, the peak strength is 93.9 MPa and the specimen also fails in shear. With the increase of confining pressure, the number of the observed fractures decreases and the peak strength increases gradually. The (σ_1–σ_3)–ε_1 curves near the peak stress become flat, and the failure modes change gradually from splitting to shear. In particular, when the confining pressure is equal to 20.0 MPa, strain hardening occurs for the SSC specimens after hydration reaction. For this case, plastic deformation occurs when the axial strain and the axial stress are 0.286% and 47.95 MPa, respectively, and strain hardening occurs when the axial strain and the axial stress are higher than 1.495% and 72.82 MPa, respectively. At an axial strain of 5.420%, the axial stress reaches the peak value of 93.9 MPa, and strain softening occurs in the post-peak deformation stage.

4 Discussions

4.1 Quantitative Analysis of Factors that Influence Expansion Pressure

Assume that the roll diameter, agent packing density, installation gap, and free expansion time are denoted as d, ρ, Δl, and t_f, respectively, and we use the dimensional analysis method (Barenblatt 1987; Szirtes 2007; Bowers and Schatzman 2009; He et al. 2018) to study the influence of those factors on the expansion pressure of the SSC quantitatively. Using the selected variables, the objective function of the expansion pressure P can be written as:

$$f\left(d, \rho, \Delta l, t_f, P\right) = 0. \tag{6}$$

Taking mass (M), length (L), and time (T) as the basic dimensions, the variables can be expressed in the power forms of the basic dimensions as:

$$\left.\begin{array}{l}[d] = M^0L^1T^0\\ [\rho] = M^1L^{-3}T^0\\ [\Delta l] = M^0L^1T^0\\ \left[t_f\right] = M^0L^0T^1\\ [P] = M^1L^{-1}T^{-2}\end{array}\right\}. \tag{7}$$

A dimensional matrix can be obtained as:

$$\boldsymbol{A}^T = \begin{bmatrix} 0 & 1 & 0 & 0 & 1\\ 1 & -3 & 1 & 0 & -1\\ 0 & 0 & 0 & 1 & -2 \end{bmatrix}. \tag{8}$$

From the dimensional harmony theorem, we have

$$[d]^{x_1}[\rho]^{x_2}[\Delta l]^{x_3}\left[t_f\right]^{x_4}[P]^{x_5} = M^0L^0T^0, \tag{9}$$

where $x_1, x_2, x_3, x_4,$ and x_5 represent the undetermined coefficients of $[d]$, $[\rho]$, $[\Delta l]$, $\left[t_f\right]$, and $[P]$, respectively.

Using matrix $\boldsymbol{X} = (x_1,\ x_2,\ x_3,\ x_4,\ x_5)^T$, Eq. (9) can be transformed into a basic solution vector for solving the linear homogeneous equations of $\boldsymbol{A}^T\boldsymbol{X} = 0$, as shown in the following equation:

$$\left.\begin{array}{l} 0\cdot x_1 + 1\cdot x_2 + 0\cdot x_3 + 0\cdot x_4 + 1\cdot x_5 = 0\\ 1\cdot x_1 - 3\cdot x_2 + 1\cdot x_3 + 0\cdot x_4 - 1\cdot x_5 = 0\\ 0\cdot x_1 + 0\cdot x_2 + 0\cdot x_3 + 1\cdot x_4 - 2\cdot x_5 = 0\end{array}\right\}. \tag{10}$$

The rank of $\boldsymbol{A}^T$ is 3 and the basic solutions of the equations of $\boldsymbol{A}^T\boldsymbol{X} = 0$ are

$$\left.\begin{array}{l} X_1 = \left(-\frac{1}{4}, -\frac{1}{2}, \frac{1}{4}, \frac{3}{4}, -\frac{1}{4}\right)^T\\ X_2 = \left(-\frac{3}{4}, \frac{1}{2}, -\frac{1}{4}, \frac{1}{4}, \frac{1}{4}\right)^T\end{array}\right\}. \tag{11}$$

Two dimensionless factors can be obtained, which are $\pi_1 = d^{-\frac{1}{4}}t_f^{-\frac{1}{2}}\rho^{\frac{1}{4}}\Delta l^{\frac{3}{4}}P^{-\frac{1}{4}}$ and $\pi_2 = d^{-\frac{3}{4}}t_f^{\frac{1}{2}}\rho^{-\frac{1}{4}}\Delta l^{\frac{1}{4}}P^{\frac{1}{4}}$. The objective function of Eq. (6) can be expressed as:

$$g\left(\pi_1, \pi_2\right) = 0. \tag{12}$$

To obtain the relation between the expansion pressure of the SSC and its influencing factors, the dimensionless factors π_1 and π_2 are calculated based on the data shown in Table 4, using the regression analysis software Origin (Norušis 2011; Egbert and Staples 2019), and the results are shown in Fig. 8. The free expansion rate refers to the expansion rate of the specimen before it contacts the boundary of the stainless-steel cylinder of the test equipment (National Development and Reform Commission 2008). The expansion rate is calculated using $\Delta l/t_f$, where Δl is the installation gap and t_f is the free expansion time.

Using the relation between the dimensionless factors shown in Fig. 8, the relation between the expansion pressure and the influencing factors is obtained as:

$$P = 0.440^2 \times d \times \rho \times \frac{\Delta L}{t_f} \times \frac{1}{t_f}. \tag{13}$$

It can be seen from Eq. (13) that the expansion pressure of the SSC is positively correlated with the roll diameter, agent packing density and free expansion rate, and negatively correlated with the free expansion time. The results shown in

Table 4 Sample data and numerical table of dimensionless factor calculation

Specimen #	Roll diameter d (mm)	Agent packing density ρ(g/cm^3)	Installation gap Δl (mm)	Free expansion time t_f (h)	Expansion pressure P(MPa)	Free expansion rate (mm/h)	π_1	π_2
A-#1	40.0	1.65	1.0	0.95	14.7	1.05	0.24	0.11
A-#2	40.0	1.85	6.0	6	2.1	0.97	0.59	0.25
A-#3	40.0	2.05	3.5	2.95	6.6	1.19	0.44	0.20
A-#4	45.0	1.65	3.5	4	3.6	0.88	0.41	0.19
A-#5	45.0	1.85	1.0	0.75	29.3	1.33	0.22	0.10
A-#6	45.0	2.05	6.0	6.5	2.9	1.00	0.55	0.24
A-#7	50.0	1.65	1.0	0.9	20.5	1.11	0.21	0.09
A-#8	50.0	1.85	3.5	2.5	10.8	1.40	0.39	0.18
A-#9	50.0	2.05	1.0	0.6	52.3	1.67	0.22	0.09

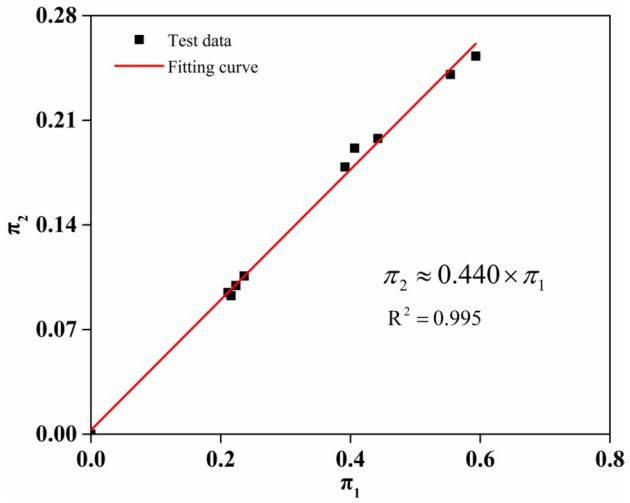

Fig. 8 Regression analysis for the dimensionless factors

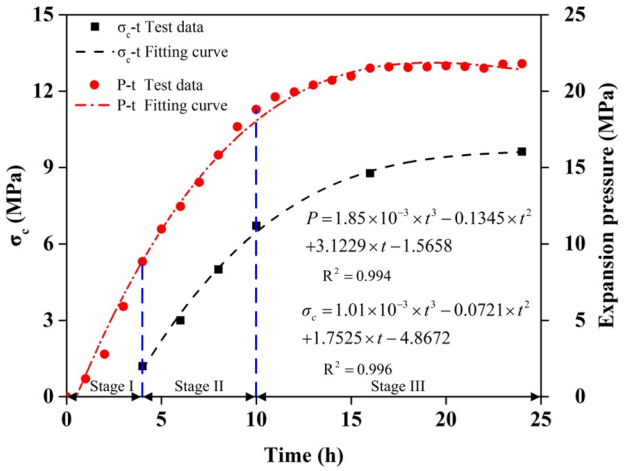

Fig. 9 σ_c–t and P–t curves and fitting formulas of SSCs

Table 4 indicate that the variation of the free expansion rate is small, which is between 0.88 and 1.67 mm/h. Hence, the free expansion time depends mainly on the installation gap, i.e., the larger the installation gap is, the longer the free expansion time and the smaller the expansion pressure will be. Therefore, the expansion pressure and the installation gap are negatively correlated with each other, and this is consistent with the test results shown in Sect. 3.2.

4.2 Time-Dependent Expansion Pressure and UCS

Based on the crystal growth theory (Chatterji 1995), the excess pressure acting on the wall of the constraint is coming from the crystal growth pressure (ΔP), which is given by

$$\Delta P = \frac{R \times T}{V_M} \times \ln \frac{a_s}{a_0}, \tag{14}$$

where V_M is the molar volume of the crystal, a_s is the mean activity of the supersaturated solution, a_0 is the mean activity of the saturated solution, R is the gas constant, and T is the absolute temperature of the system.

During the hydration reaction, the activity of an oversaturated solution (a_s) and the absolute temperature of the system (T) change continuously. The pressure increment (ΔP) due to the crystallization of $Ca(OH)_2$ varies accordingly, which can lead to a variation of the expansion pressure and the peak strength of the specimen with reaction time. The UCS and the expansion pressures of the SSC specimens (with an agent packing density of 1.65 g/cm^3) at different reaction times (4, 6, 8, 10, 16 and 24 h) are used to plot the σ_c–t and the P–t curves shown in Fig. 9.

The hydration reaction process of the SSC specimens can be divided into three stages: the initial stage ($t \le 4$ h) in which the expansion pressure grows rapidly, the middle stage (4 h $< t \le 10$ h) in which the growth rate of the expansion pressure decreases, and the final stage ($t \ge 10$ h) in which the expansion pressure increases slowly. The expansion pressure

increases with the reaction time at a power of three. The reason is that in the initial stage, heat is released rapidly and the $Ca(OH)_2$ crystals are generated quickly due to the hydration reaction. This leads to a rapid increase of the activity of the oversaturated solution and the absolute temperature of the system. As a result, in the initial stage of the hydration reaction, the ΔP increase rate is high, and the expansion pressure increases rapidly. With the increase of the reaction time ($4\ \text{h} < t \leq 10\ \text{h}$), the rates of heat release and $Ca(OH)_2$ crystal growth decrease gradually. This leads to a gradual decrease of the activity of the oversaturated solution and the absolute temperature of the system, which results in a continuous decrease of the rate of expansion pressure increase. The growth rate of the expansion pressure decelerates in this stage. In the final stage of the hydration reaction ($t \geq 10$ h), the rates of heat release and $Ca(OH)_2$ crystal growth further decrease, leading to a further decrease of the activity of the oversaturated solution and the absolute temperature of the system. As a result, the rate of expansion pressure increase further decreases and approaches zero in the end.

The mechanism of expansion pressure development of the SSC specimens can be used to explain the increase of E and the decrease of ν over the time of hydration reaction. As shown in Fig. 10, as the hydration reaction time increases, the elastic modulus increases while the Poisson's ratio decreases. When the reaction time is less than 6 h, the elastic moduli and the Poisson's ratios of the SSC specimens, respectively, increase and decrease quickly with the hydration reaction time. The elastic moduli and Poisson's ratios are 0.20 GPa and 0.30, 0.42 GPa and 0.26, respectively, for hydration reaction times of 4 h and 6 h. The growth rate of the $Ca(OH)_2$ crystals is relatively fast in the initial stage of hydration reaction. In a constraint space, the internal pores in the specimen are crushed quickly and the SSC is compacted continuously. This is why there is a gradual increase of elastic modulus and decrease of Poisson's ratio. When the hydration reaction time is 8 h, the elastic modulus and the Poisson's ratio are 0.58 GPa and 0.22, respectively. When the reaction time is 10 h, the elastic modulus and the Poisson's ratio change to 0.80 GPa and 0.20, respectively. The generation rate of the $Ca(OH)_2$ crystals decelerates in the middle stage of the hydration reaction. As a result, the rate of the collapse of internal pores in the specimen decreases, leading to a gradual decrease of the compaction rate of the SSC and a decrease of the rates of change of the elastic modulus and the Poisson's ratio over hydration reaction time. If the hydration reaction time is more than 10 h, the rates of change of the elastic modulus and Poisson's ratio over hydration reaction time further decrease. When the hydration reaction time is 16 h, the elastic modulus and the Poisson's ratio are 1.20 GPa and 0.19, respectively. In comparison, when the hydration reaction time is 24 h, the elastic modulus and the Poisson's ratio are 1.24 GPa and 0.18, respectively. There are only slight changes of the elastic modulus and the Poisson's ratio for a difference of 8 h of hydration reaction time. In the final stage of hydration reaction, the growth rate of the $Ca(OH)_2$ crystals further decreases and the internal pores in the specimen are completely filled. As a result, the elastic modulus and the Poisson's ratio vary very little and approach their respective stable values.

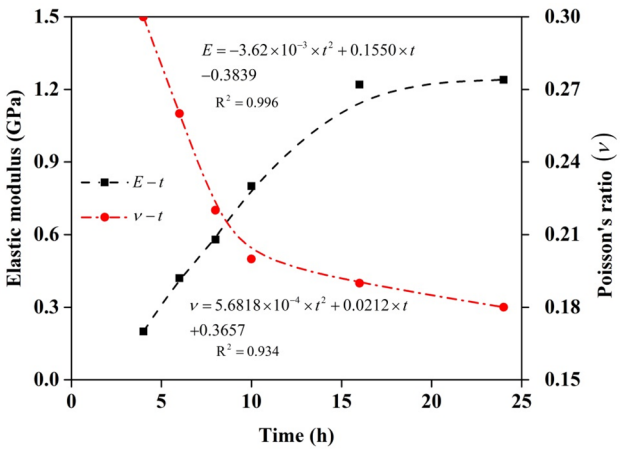

Fig. 10 E–t and ν–t curves as well as fitting formulas of SSCs

It is seen that the evolution of the expansion pressure of the SSCs can be used to explain the increase of elastic modulus and the decrease of Poisson's ratio with hydration reaction time. Empirical formulas of the σ_c–t, P–t, E–t, and ν–t curves are given in Figs. 9 and 10, which can be used in numerical modeling to further study the expansion mechanism of the SSCs.

4.3 Failure Criterion

With a failure criterion in place, mechanical property parameters can be obtained, which can be used in numerical simulation of the SSCs in field application. Using the Mohr–Coulomb failure criterion, the relation between the shear stress τ and the normal stress σ_n acting on a shear plane is

$$\tau = c + \sigma_n \times \tan\phi, \tag{15}$$

where c is the cohesion and ϕ is the internal friction angle.

Assume that the angle between the shear plane and the horizontal is θ, as shown in Fig. 11, then τ and σ_n can be represented by the maximum σ_1 and the minimum σ_3 principal stresses as:

$$\left.\begin{aligned}\sigma_n &= \frac{1}{2}\times(\sigma_1+\sigma_3) + \frac{1}{2}\times(\sigma_1-\sigma_3)\times\cos 2\theta\\ \tau &= \frac{1}{2}\times(\sigma_1-\sigma_3)\times\sin 2\theta\end{aligned}\right\}. \tag{16}$$

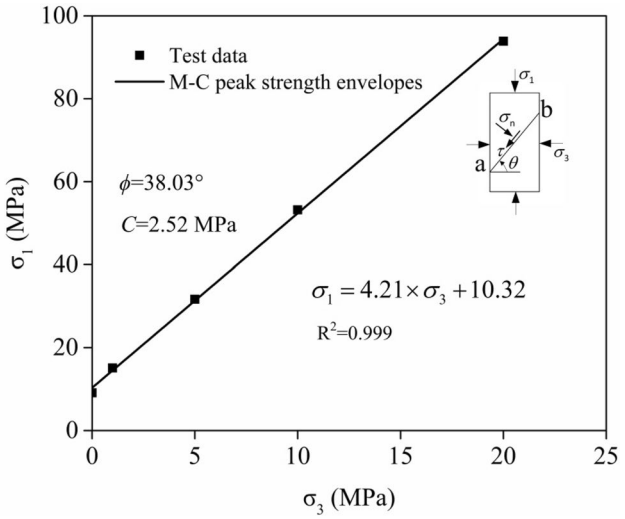

Fig. 11 M–C peak strength envelope and fitting formula for SSC

Combining Eqs. (15) and (16), the Mohr–Coulomb failure criterion can be expressed as:

$$\sigma_1 = \frac{1+\sin\phi}{1-\sin\phi} \times \sigma_3 + \frac{2c \times \cos\phi}{1-\sin\phi}. \tag{17}$$

For $\sigma_3 = 0$, we obtain the uniaxial compressive strength, which is

$$\sigma_c = \frac{2c \times \cos\phi}{1-\sin\phi}. \tag{18}$$

The relation between θ and ϕ is

$$\frac{1+\sin\phi}{1-\sin\phi} = \tan^2\theta. \tag{19}$$

Substituting Eqs. (19) and (18) into Eq. (15), we have

$$\sigma_1 = \sigma_3 \times \tan^2\theta + \sigma_c. \tag{20}$$

Based on the test data shown in Fig. 7, the parameters for the Mohr–Coulomb failure criterion are calculated as $c = 2.52$ MPa and $\phi = 38.03°$. Thus, the Mohr–Coulomb failure criterion for the SSC is

$$\sigma_1 = 4.21 \times \sigma_3 + 10.32\,(\text{MPa}). \tag{21}$$

Using the Mohr–Coulomb failure criterion, the relation between the shear stress τ and the normal stress σ_n acting on a shear plane is

$$\tau = 0.7822 \times \sigma_n + 2.52\,(\text{MPa}). \tag{22}$$

Table 5 Mechanical properties of standard concrete specimens

Test number	σ_{cc} (MPa)	σ_{tc} (MPa)	E_c (GPa)	ν_c
C-#1	31.3	2.59	30.18	0.271
C-#2	33.2	2.49	30.25	0.264
C-#3	30.4	2.63	30.34	0.266
Average value	31.6	2.54	30.26	0.267

σ_{cc} is the uniaxial compressive strength; σ_{tc} is the tensile strength; E_c and ν_c are the Young's modulus and Poisson's ratio of the concrete, respectively

4.4 Fracturing Performance of SSC

To further understand the fracturing performance of SSC, a concrete block, which has a dimension of 300 mm (length) × 300 mm (height) × 250 mm (thickness), was used for breakage test. There was a 52.0-mm circular hole in the center of the block in the thickness direction. Through uniaxial compression and Brazilian tests, the mechanical properties of the concrete were obtained and shown in Table 5.

A SSC with a diameter of 50.0 mm, a length of 100.0 mm and a density of 1.65 g/cm^3 was soaked in 20 °C water for 9 min. After the SSC was saturated with water, it was placed in the center position of the hole in the concrete block. In the process of testing, the surface deformation of the concrete block was measured using a Digital Image Correlation Measurement System (DICMS) (Peng et al. 2019; Zhang et al. 2019) to obtain the surface strain, and crack propagation during the fracturing process was recorded using photoimages.

The test result is shown in Fig. 12. When the hydration reaction time was 0.7 h, the calculated expansion pressure generated by the SSC was 0.55 MPa according to the fitting formula in Fig. 9. At this time, stress concentration appeared on the surface of the concrete block near the hole perimeter, and the maximum principal strain was about 0.26–0.27%. When the hydration reaction time increased to 1 h, the calculated expansion pressure of the SSC was 1.42 MPa. The strains on the surface of the concrete block increased in the vertical centerline, and the maximum principal strains ranged from 0.33 to 0.36%. Spalling occurred in the lower half of the specimen. With further hydration reaction, the principal strains along the vertical center line increased. When the hydration reaction time was 1.5 h, the calculated expansion pressure reached 2.88 MPa, which exceeded the tensile strength of the concrete ($\sigma_{tc} = 2.54$ MPa). The concrete block cracked along the vertical centerline. When hydration reaction time was 4.0 h, the crack width reached 20.4 mm. The maximum crack width reached 30.6 mm when the hydration reaction time was more than 24 h (Fig. 12).

The results of the laboratory fracturing test of the concrete block using SSC show that the expansion pressure

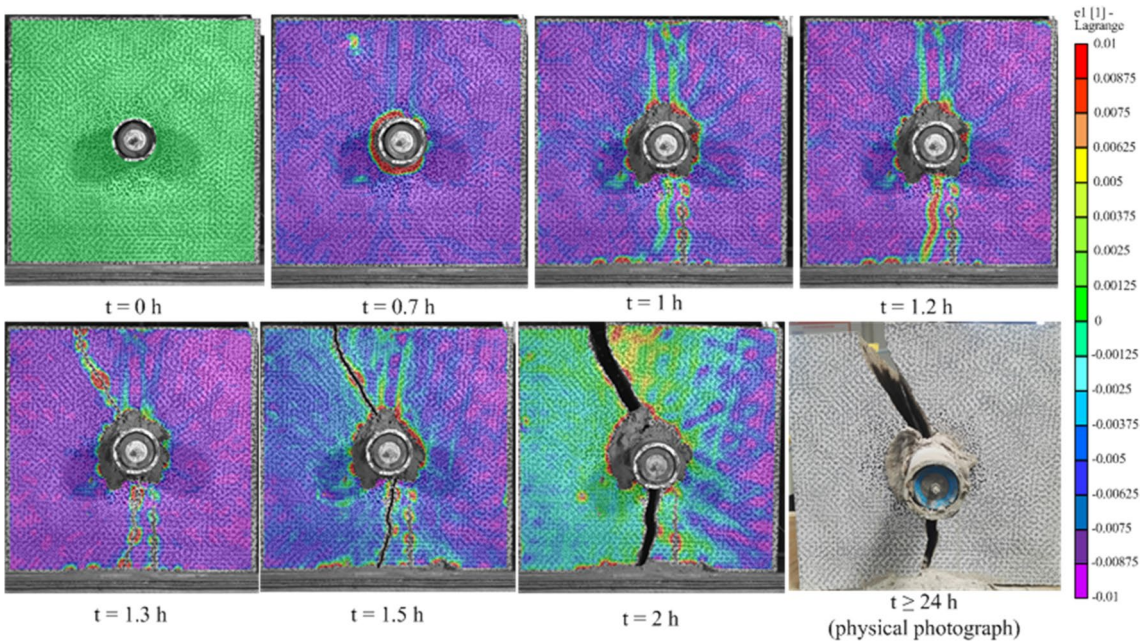

Fig. 12 Cracking process of concrete based on DICMS

produced by SSC increases with the increase of hydration reaction time. Under the expansion pressure of SSC, spalling failure occurred in the concrete block in 1 h, microcracks were observed in 1.3 h, and macrocracks appeared in 1.5 h. The crack width reached 20.4 mm in 2 h. This demonstrates that the SSC has a good cracking performance and a high cracking efficiency, and it can be used for concrete demolition and rock fracturing. In addition, the expansion pressure of SSC can be calculated using the fitting formula of the mechanical and expansion properties under different hydration reaction time and confining pressure. Combined with the mechanical properties of the objects to be fractured (e.g., rock or rock mass), de-stress in highly stressed brittle rock can be carried out by fracturing the rock using the SSCs to reduce rock burst risk. They can also be used in other engineering applications such as secondary breakage of rocks. Furthermore, the developed SSCs can be used to fracture rock in wet boreholes or up-tilt boreholes. We plan to conduct field experiments of rock fracturing using the developed SSC in our future studies.

5 Conclusions

Water absorption, expansion pressure and mechanical property tests of specimens of the novel SSC after hydration reaction were carried out in this study. The following conclusions are made based on the test results.

The water absorption and the water absorption rate of the newly developed SSC decrease as the agent packing density increases. A SSC can be fully saturated after immersing it in 20 °C water for 9–13 min. The water absorption is between 20 and 25%, which is close to the optimal water to cement ratio of 25% of SCDAs. The recommended agent packing density is 1.65 g/cm^3, at which the immersion time and the water absorption are 9 min and 22%, respectively.

The expansion pressure of the SSC is positively correlated with the roll diameter and the agent packing density and negatively correlated with the insertion gap. The expansion pressure is most sensitive to insertion gap and least sensitive to roll diameter. A mathematical model relating the expansion pressure and its influencing factors is established through dimensional analysis and regression analysis.

When the reaction time is less than 24 h, both UCS and elastic modulus of the SSC after hydration reaction increase with the hydration reaction time, while the Poisson's ratio decreases with the hydration reaction time. When the hydration reaction time is 24 h, the UCS, expansion pressure, elastic modulus and Poisson's ratio approach their corresponding stable values, which are 9.6 MPa, 20.5 MPa, 1.24 GPa and 0.18, respectively. With the increase of confining pressure, the peak strength of the SSC increases linearly. The cohesion and the internal friction angle for the Mohr–Coulomb failure criterion are 2.52 MPa and 38.01°, respectively.

The application of the newly developed SSC is easy and the SCDA paste is less likely to be extruded from boreholes. It can be applied to fracturing rock masses using boreholes in any inclination, dry or wet. This is important for broadening the application of SCDAs. In future studies, we will investigate the expansion and strength characteristics of the

SSC in complex underground environments with chemical water and extreme (high or low) temperatures.

Acknowledgements This study was funded by the State Key Research Development Program of China (2018YFC0604400), the National Science Foundation of China (51874068, 51974061), the Fundamental Research Funds for the Central Universities (N160107001, N180701016, N2001003), and the 111 Project (B17009).

Compliance with Ethical Standards

Conflict of interest The authors declare that they have no conflict of interests.

References

Fairhurst C, Hudson J (1999) Draft ISRM suggested method for the complete stress-strain curve for intact rock in uniaxial compression. Int J Rock Mech Min Sci 36:279–289

Arshadnejad S, Goshtasbi K, Aghazadeh J (2011) A model to determine hole spacing in the rock fracture process by non-explosive expansion material. Int J Miner Metall Mater Struct 18:509–514

Ba H, Liu Q (1988) Research on several problems of static blasting agent. J Wuhan Univ Technol 2:61–68

Barenblatt GI (1987) Dimensional analysis. CRC Press, Boca Raton

Bowers B, Schatzman L (2009) Dimensional analysis in developing grounded theory: the second generation. Left Coast Press, California

Chatterji S (1995) Mechanism of expansion of concrete due to the presence of dead-burnt CaO and MgO. Cem Concr Res 25:51–56

Chatterji S, Jeffery J (1966) The volume expansion of hardened cement paste due to the presence of "dead-burnt" CaO. Mag Concr Res 18:65–68

China NDaRCo (2008) Soundless cracking agent. Building Materials Industry Press, Beijing

Dai X (2016) Development of loading system using static cracking agent for blasting failure law of brittle material in high stress. Doctoral dissertation, Northeastern University

De Silva RV, Pathegama Gamage R, Perera A, Samintha M (2016) An alternative to conventional rock fragmentation methods using SCDA: a review. Energies 9:958–989

De Silva VRS, Ranjith PG, Perera MSA, Wu B, Rathnaweera TD (2017) Investigation of the mechanical, microstructural and mineralogical morphology of soundless cracking demolition agents during the hydration process. Mater Charact 130:9–24

De Silva V, Ranjith P, Perera M, Wu BJJoNGS, (2019) The effect of saturation conditions on fracture performance of different soundless cracking demolition agents (SCDAs) in geological reservoir rock formations. J Nat Gas Sci Eng Geol 62:157–170

Deighton M (1976) Fracture of brittle solids. Phys Bull 27:220–221

Egbert J, Staples S (2019) Doing multi-dimensional analysis in SPSS, SAS, and R. In: Sardinha TB, Pinto MV (eds) Multi-dimensional analysis : research methods and current issues, 1st edn. Bloomsbury Academic, London, pp 125–144

Étkin M, Azarkovich A (2006) Effect of non-explosive splitting compounds and rational work parameters. Power Technol Eng 40:287–292

Gambatese JA (2003) Controlled concrete demolition using expansive cracking agents. J Constr Eng Manag 129:98–104

Guo T, Zhang S, Ge H, Qu Z (2015) A **novel" soundless cracking agent fracturing" for shale gas reservoir stimulation. Int J Environ Sci Dev 6:681–687

Guo T, Zhang S, Ge H, Wang X, Lei X, Xiao B (2015) A new method for evaluation of fracture network formation capacity of rock. Fuel 140:778–787

Harada T, Idemitsu T, Watanabe A, Takayama S-I (1989) The design method for the demolition of concrete with expansive demolition agents. In: Shah SP, Swartz SE (eds) Fracture of concrete and rock. Springer, New York, pp 47–57

Harada T, Soeda K, Idemitsu T, Watanabe A (1993) Characteristics of expansive pressure of an expansive demolition agent and the development of new pressure transducers. Doboku Gakkai Ronbunshu 1993:91–100

He Q, Suorineni F, Oh J (2016) Review of hydraulic fracturing for preconditioning in cave mining. Rock Mech Rock Eng 49:4893–4910

He Q, Suorineni F, Oh JJRM (2017) Strategies for creating prescribed hydraulic fractures in cave mining. Rock Mech Rock Eng 50:967–993

He Q, Suorineni FT, Ma T, Oh J (2018) Parametric study and dimensional analysis on prescribed hydraulic fractures in cave mining. Tunn Undergr Space Technol 78:47–63

Hertzberg RW, Saunders H (1985) Deformation and fracture mechanics of engineering materials (2nd edition). J Press Vessel Technol Trans ASME 107:309–311

Huynh M-P, Laefer DF (2009) Expansive cements and soundless chemical demolition agents: state of technology review. In: The 11th conference on science and technology, Ho Chi Minh City Vietnam, October 21–23, 2009

Kasai Y (1989) The Second International RILEM Symposium on demolition and reuse of concrete and masonry. Mater Struct 22:312–319

Kasama T, Saito T, Wada M (1983) Hydration-expansive crushing cartridge. U.S. Patent

Kim K, Cho H, Sohn D, Koo J, Lee J (2018) Prediction of the minimum required pressure of soundless chemical demolition agents for plain concrete demolition. J Comput Struct Eng Inst Korea 31:251–258

Kovari K, Tisa A, Einstein HH, Franklin JAJIJoRM (1983) Suggested methods for determining the strength of rock materials in triaxial compression: revised version. Int J Rock Mech Min Sci Geomech Abstr 20:283–290

Laefer DF, Ambrozevitch-Cooper N, Huynh M, Midgette J, Ceribasi S, Wortman J (2010) Expansive fracture agent behaviour for concrete cracking. Mag Concr Res 62:443–452

Lawn B (1993) Fracture of brittle solids. Cambridge University Press, Cambridge

Li Y, Li K, Feng X, Cai M (2018) Development and evaluation of artificial expandable pillars for hard rock mining. Int J Rock Mech Min Sci 110:68–75

National Development and Reform Commission PsRoC (2008) Soundless cracking agent vol JC 506-2008. Building Materials Industry Press, Beijing

Norušis MJ (2011) IBM SPSS statistics 19 guide to data analysis. Prentice Hall Upper Saddle River, New Jersey

Pawlik PS, Reisman H (1980) Elasticity: theory and applications. Wiley, New York

Peng J, Zhang F, Yan G, Qiu Z, Dai X (2019) Experimental study on rock-like materials fragmentation by electric explosion method under high stress condition. Powder Technol 356:750–758

Ramachandran VS, Sereda PJ, Feldman R (1964) Mechanism of hydration of calcium oxide. Nature 201:288–289

Shang J, Zhao Z, Aliyu M (2018) Stresses induced by a demolition agent in non-explosive rock fracturing. Int J Rock Mech Min Sci 107:172–180

Swanson D, Labuz J (1999) Behavior of a calcium oxide-based expansive cement. Concr Sci Eng 1:166–172

Szirtes T (2007) Applied dimensional analysis and modeling. Butterworth-Heinemann, Oxford

Xie B, Yan Z, Zhao Z (2018) Experimental study on anti-spraying hole of static blasting based on physical cooling. J Saf Sci Technol 14:150–154

Xu QJ, Jiang N, Long Y, Liao Y, Yang T, Ji R, Liu D (2015) Investigation of the large scale borehole soundless cracking experiment on the concrete members. In: Applied mechanics and materials, 2015. Trans Tech Publ, pp 219–226

Xu S, Hou P, Cai M, Li Y (2019) An experiment study on a novel self-swelling anchorage bolt. Rock Mech Rock Eng 52:4855–4862

You B (2008) Static blasting technology: soundless chemical agent and its application. China Building Materials Press, Beijing

Zhai C, Xu J, Liu S, Qin L (2018) Fracturing mechanism of coal-like rock specimens under the effect of non-explosive expansion. Int J Rock Mech Min Sci 103:145–154

Zhang F, Yan G, Peng J, Qiu Z, Dai X (2019) Experimental study on crack formation in sandstone during crater blasting under high geological stress. Bull Eng Geol Environ 79:1323–1332